Investigation of oxygen reduction reaction kinetics on $Sm_{0.5}Sr_{0.5}CoO_{3-\delta}$ cathode supported on $Ce_{0.85}Sm_{0.075}Nd_{0.075}O_{2-\delta}$ electrolyte

Zhan Gao [a,b,*], Xingmin Liu [b], Bill Bergman [a], Zhe Zhao [a,b,*]

[a] Department of Materials Science and Engineering, Royal Institute of Technology (KTH), SE 10044 Stockholm, Sweden
[b] Department of Materials and Environmental Chemistry, Arrhenius Laboratory, Stockholm University, SE 10691 Stockholm, Sweden

ABSTRACT

$Sm_{0.5}Sr_{0.5}CoO_{3-\delta}$ (SSC) cathode prepared by a glycine–nitrate process (GNP) is investigated for solid oxide fuel cells (SOFCs) based on $Ce_{0.85}Sm_{0.075}Nd_{0.075}O_{2-\delta}$ (SNDC) electrolyte. SSC forms cubic perovskite structure after being annealed at 1100 °C for 5 h. SSC cathode and SNDC electrolyte can retain their own structure and there is no reaction between the two compositions. The microstructure of the cathode and the interfaces between cathodes and SNDC electrolytes are studied by scanning electron microscopy (SEM) after sintering at various temperatures. Impedance spectroscopy measurements reveal that area specific resistances (ASRs) of SSC–SNDC30 cathode are much lower than those of SSC cathode. Kinetics of oxygen reduction reaction (ORR) on porous SSC cathode is investigated by analysis of impedance spectra. Medium-frequency conductivities show no dependency on oxygen partial pressure (P_{O_2}), which can be attributed to the oxygen ions transfer across the electrode/electrolyte interface. The dependencies of low-frequency conductivities on oxygen partial pressure (P_{O_2}) vary in the range from *ca.* 0.31 to *ca.* 0.34 and increase with the increasing temperatures. The low-frequency electrode process is a mixing process involving oxygen reduction reaction related to atomic oxygen and oxygen ions conduction step together with total charge-transfer step. IR-compensated current density (i)–overpotential (η) relationship is established and the exchange current densities i_o originated from high-field approximations are much higher than those of low-field approximations and a.c. impedance data under OCV state. It demonstrates the polarization overpotential has great effect on the kinetics of ORR. The polarization current is observed to increase with time in the long-term stability measurement, which can be ascribed to the propagation process of oxygen vacancies.

© 2011 Elsevier B.V. All rights reserved.

1. Introduction

Solid oxide fuel cells (SOFCs) convert chemical energy to electrical power with high efficiency and low emissions. Recently, most research has focused on low to intermediate-temperature SOFCs (500–800 °C) since they facilitate the use of metallic interconnects together with versatile seals and improve the long-term stability. However, the fuel cell performance dramatically decreases with the lowering operating temperature, mainly ascribed to the ohmic losses of the electrolyte and deterioration of electrochemical activity of cathode [1,2].

Ohmic polarization of electrolyte can be greatly improved by utilizing novel electrolyte materials with high ionic conductivity and thin-film technique. Ceria-based solid solution has been widely accepted as a suitable alternative to yttria-stabilized zirconia (YSZ). However, singly doped ceria suffers from the reduction of Ce^{4+} to Ce^{3+} at low oxygen partial pressures, which results in electronic conduction causing a loss in power output [2]. In addition, the grain-boundary resistivity is extraordinarily high at reduced temperatures. Co-doping strategies have been utilized to improve the properties of ceria-based electrolyte and enhancement of ionic conductivity has been observed [3–5]. Among varieties of co-doped ceria electrolytes, Sm^{3+} and Nd^{3+} co-doped ceria with the composition of $Ce_{0.85}Sm_{0.075}Nd_{0.075}O_{2-\delta}$ (SNDC) exhibits promising performance [3]. However, there is lack of information on the compatible cathodes with the $Ce_{0.85}Sm_{0.075}Nd_{0.075}O_{2-\delta}$ electrolyte.

It is critical to exploit an ideal cathode with high electronic and ionic conductivity in addition to high catalytic and electrochemical activity for the oxygen reduction reaction (ORR). Mixed ionic and electronic conducting (MIEC) perovskite-type oxides have been investigated as cathode materials for low-temperature SOFCs in the past decades and conspicuous performances have been achieved [1,6–11]. Among varieties of MIEC cathodes, $Sm_{0.5}Sr_{0.5}CoO_{3-\delta}$ (SSC) cathode demonstrates excellent electrocatalytic activity and

* Corresponding authors at: Department of Materials Science and Engineering, Royal Institute of Technology (KTH). SE 10044 Stockholm, Sweden.
Tel.: +46 08 7908354; fax: +46 08 207681.
E-mail addresses: zhangao@kth.se (Z. Gao), zhezhao@kth.se (Z. Zhao).

performances [7]. Several studies concerning the kinetics of ORR on SSC cathode have been reported. Baek et al. investigated cathode reaction mechanism of porous $Sm_{0.5}Sr_{0.5}CoO_{3-\delta}/Sm_{0.2}Ce_{0.8}O_{1.9}$; oxygen ion conduction in the bulk cathode and gas phase diffusion of oxygen was the dominant processes based on the impedance spectra analysis using series equivalent circuit [12]. Baumann et al. studied the dense thin-film microelectrode and found the oxygen exchange reaction on the $Sm_{0.5}Sr_{0.5}CoO_{3-\delta}$ cathode dominated the ORR kinetics [13]. Adler et al. developed a continuum model to analyze the mechanism of ORR on porous MIEC cathodes and found the solid-state oxygen diffusion and oxygen surface exchange reaction dominated the electrochemical behavior [14]. However, research from Wang et al. illustrated the mechanism of ORR on $Sm_{0.5}Sr_{0.5}CoO_{3-\delta}$ cathode was determined strongly by the reaction conditions [15]. Koyama et al. proposed a model to study the porous SSC cathode with high ionic conductivity. The model takes the processes of (i) diffusion of oxygen in the gas phase, (ii) surface adsorption/desorption process, and (iii) ionic conduction in the bulk SSC into account. The three processes correspond to the low-frequency, medium-frequency, and high-frequency arcs in impedance spectra. The low-frequency, medium-frequency, and high-frequency specific electrode conductivities are proportional to $P_{O_2}^1$, $P_{O_2}^{1/2}$, $P_{O_2}^{1/4}$, respectively [16].

Although many studies on SSC cathode have been performed so far, little information about the characteristics of SSC supported on the $Ce_{0.85}Sm_{0.075}Nd_{0.075}O_{2-\delta}$ electrolyte is available. In this work, SSC is investigated as promising compatible cathode with the SNDC electrolyte and the electrochemical kinetics of ORR on SSC cathode are presented.

2. Experimental

2.1. Electrolyte preparation

$Ce_{0.85}Sm_{0.075}Nd_{0.075}O_{2-\delta}$ (SNDC) was synthesized by an oxalate coprecipitation process. $Ce(NO_3)_3 \cdot 6H_2O$ (99.9%, Alfa Aesar), $Sm(NO_3)_3 \cdot 6H_2O$ (99.9%, Alfa Aesar) and $Nd(NO_3)_3 \cdot 6H_2O$ (99.9%, Alfa Aesar) were used as the starting materials. The stoichiometric starting materials were dissolved in the distilled water, and then the solution was dripped to the oxalic acid solution, which was adjusted to neutral pH (6.6–6.9) by dilute ammonia solution. After the precipitate was fully washed by water and ethanol, it was calcined at 700 °C for 2 h. Pellets with about 10 mm in diameter and 1 mm in thickness were prepared by uniaxially pressing SNDC powder and sintering at 1500 °C for 5 h.

2.2. Cathode preparation

$Sm_{0.5}Sr_{0.5}CoO_{3-\delta}$ (SSC) cathode was prepared by using a glycine–nitrate process (GNP). Stoichiometric amount of Sm_2O_3 (99.9%, Alfa Aesar), $Sr(NO_3)_2$ (99.9%, Alfa Aesar) and $Co(NO_3)_2$ (99.9%, Alfa Aesar) was dissolved in dilute nitric acid. Glycine (99.9%, Alfa Aesar) was introduced to the solution with molar ratio of glycine:nitrate of 1:2 under heating and stirring. It was then boiled to evaporate excess water in a hot plate. The solution converts to viscous gel and ignites to combustion, resulting in an oxide ash. The ash was finally annealed at 1100 °C for 5 h in air to remove carbon residues and form a well-crystalline structure. To examine the phase reactivity between SSC cathode and SNDC electrolyte, the two components are mixed thoroughly and sintered at 1200 °C for 5 h.
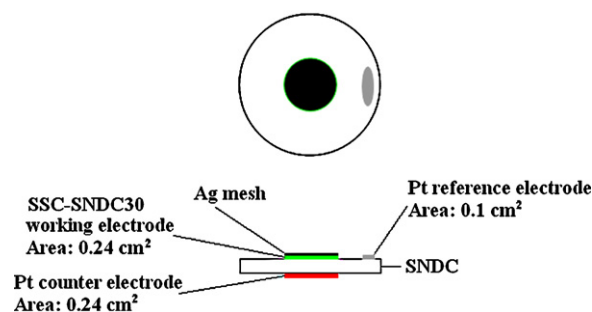

Fig. 1. Schematic diagram of three-electrode setup.

2.3. Symmetric cell construction

Slurries of $Sm_{0.5}Sr_{0.5}CoO_{3-\delta}$ cathode and $Sm_{0.5}Sr_{0.5}CoO_{3-\delta}$–$Ce_{0.85}Sm_{0.075}Nd_{0.075}O_{2-\delta}$ (30 wt.%) cathode, identified as SSC and SSC–SNDC30, respectively, were prepared by ball-milling the powders, terpineol and ethylcellulose for 24 h. The slurries were subsequently coated onto both sides of the SNDC pellets by screen-printing technique to form symmetric cells. The coated electrode layer was dried at 150 °C for 2 h and subsequently fired at 1000, 1100 and 1200 °C for 5 h in air, respectively.

2.4. Half-cell construction

A schematic diagram of three-electrode configuration is shown in Fig. 1. SSC–SNDC30 slurry was screen-printed on a masked SNDC electrolyte as working electrode (WE). The mask was removed after the slurry was dried in the oven at 100 °C for 1 h. The cathode on the electrolyte was sintered at 1100 °C for 5 h. The effective electrode area was 0.24 cm². Pt electrodes, prepared by painting Pt paste on electrolyte and sintered at 800 °C for 2 h, were used as reference electrode (RE) and counter electrode (CE). Reference electrode located at the same side of working electrode and was 3 mm away from the working electrode. Counter electrode located symmetrically at the opposite side of working electrode. Such arrangement was chosen to minimize the misalignment error of working electrode and counter electrode [17,18].

2.5. Electrochemical measurement

Cyclic voltammetry (CV) measurements between +0.1 V and −0.7 V vs. RE with scan rate of 5 mV s⁻¹ were performed using an IM6ex electrochemical workstation (Zahner IM6ex, Germany). A.c. impedance measurement was performed in the frequency range of 100 kHz–100 mHz with an excitation voltage of 10 mV under open-circuit voltage (OCV) state. A.c. impedance was conducted under different oxygen partial pressures (P_{O_2}) from 1 atm, 0.5 atm, 0.21 atm, 0.105 atm to 0.05 atm. Different oxygen partial pressures were realized by pre-mixing O_2 and N_2 controlled by the mass flowmeter with total volumetric flow rate of 240 mL min⁻¹ under 1 atm pressure.

Impedance spectra were analyzed by a non-linear least squares program handled by ZSimpwin software. To establish resistance-free current density (i)–overpotential (η) characteristics, IR drop originated from the electrolyte resistance between the working electrode and reference electrode was compensated for by post-factum correction of the CVs using series resistances obtained from impedance data. The overpotential of the cathode under cathodic polarization was calculated by the following equation [19]:

$$\eta = E - I \times R_s \tag{1}$$
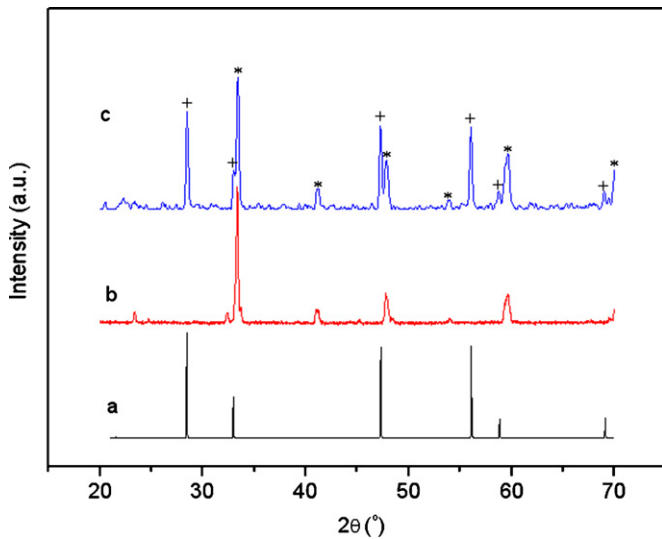
Fig. 2. XRD patterns of (a) SNDC sintered at 1500 °C for 5 h, (b) SSC sintered at 1100 °C for 5 h, (c) SSC–SNDC30 composite cathode sintered at 1200 °C for 5 h. (*) is for SSC phase, and (+) is for SNDC phase.

where η, E, I and R_s represent the overpotential of cathode, applied cathodic voltage, polarization current and series resistance, respectively.

### 2.6. Microstructure characterizations

X-ray diffraction (XRD) was performed by using a PANalytical X'pert Pro diffractometer equipped with Cu target operating at voltage and current of 40 kV and 40 mA. The microstructure of cathode was detected by scanning electron microscope (SEM, JSM-7000F, JEOL Ltd., Japan).

3. Results and discussion

3.1. Microstructure characterization

Fig. 2 illustrates the XRD patterns for different specimens. The SSC powder sintered at 1100 °C for 5 h has formed crystalline with cubic perovskite structure. The SNDC appears cubic fluorite structure. In the XRD pattern of SSC–SNDC30 cathode, SSC and SNDC in the composites retain their own structures. Stable phases do not form via solid state reaction after SSC–SNDC30 cathode being sintered at 1200 °C for 5 h.

Fig. 3 presents the SEM cross-sectional morphologies of different cathodes. Generally, the increasing sintering temperature
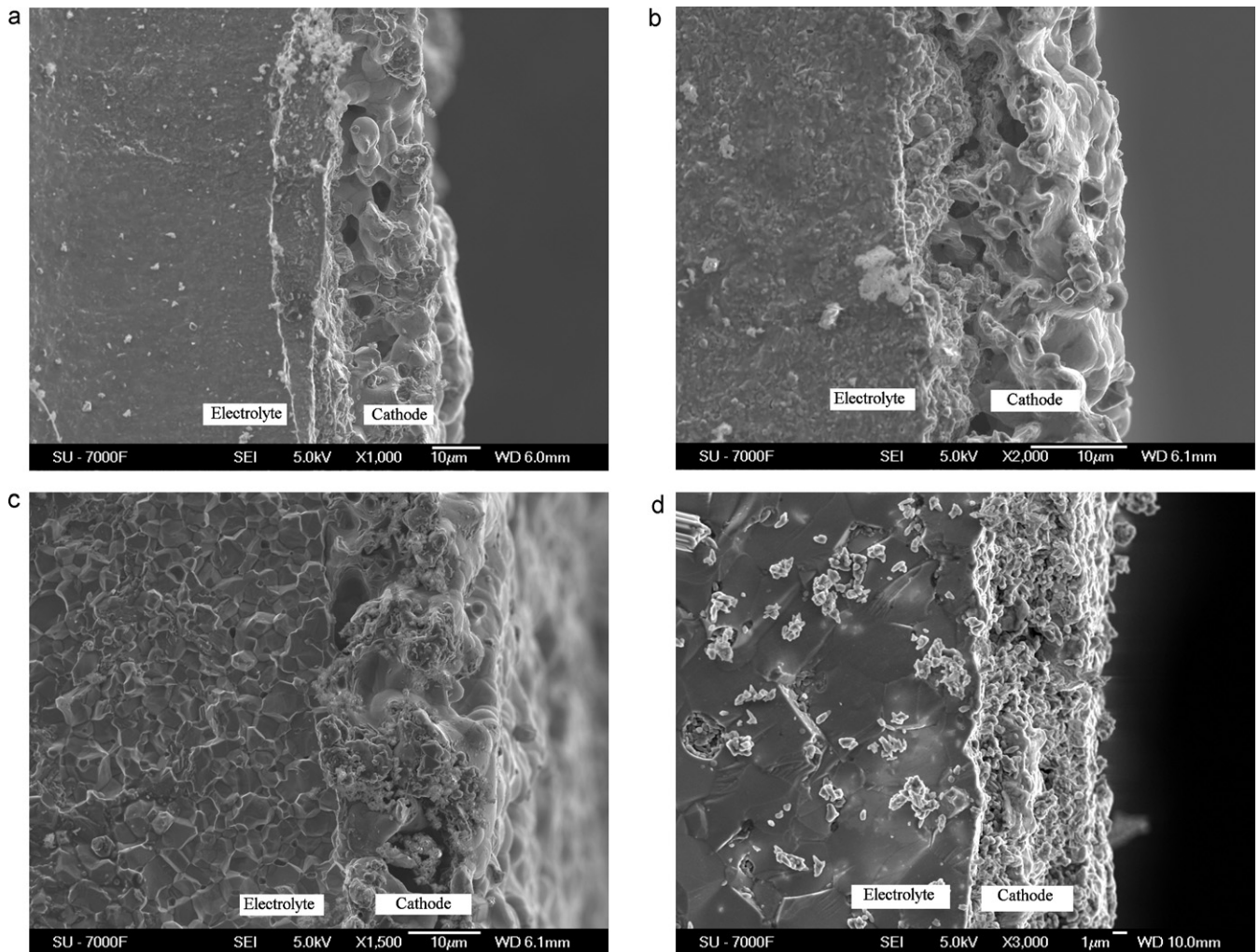
Fig. 3. SEM cross-sectional images for (a) SSC sintered at 1000 °C for 5 h, (b) SSC sintered at 1100 °C for 5 h, (c) SSC sintered at 1200 °C for 5 h, and (d) SSC–SNDC30 sintered at 1100 °C for 5 h.
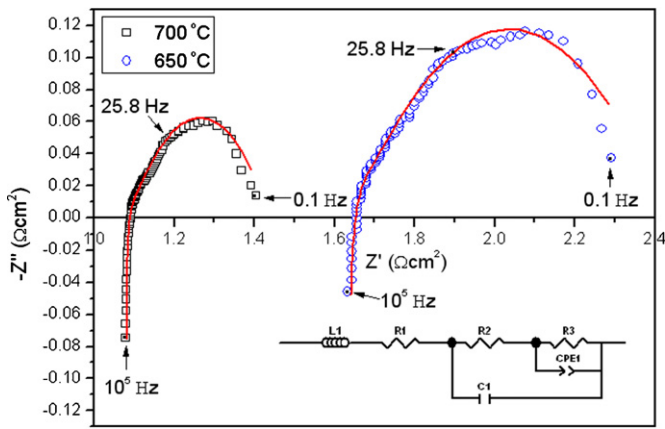
Fig. 4. A.c. impedance spectra for SSC–SNDC30 cathode measured at 650 °C and 700 °C under atmospheric pressure. Insert is the equivalent circuit employed to fit the impedance spectra. The solid lines are fitting curves.

enhances the sinterability of cathode particles and adhesion to the electrolyte, which ensures a better contact with the electrolyte and a better current collection. However, it reduces the cathode porosity, which decreases the electrode surface area-gas solid interface (triple phase boundaries, TPBs), resulting in high interfacial polarization resistance. Therefore, obtaining cathodes with fine microstructures and strong adhesion to electrolyte with respect to sintering temperatures is a trade-off relationship. As presented in Fig. 3a, the SSC cathode sintered at 1000 °C exhibits poorer contact to the electrolyte compared with the cathode sintered at 1100 °C and 1200 °C. However, SSC sintered at 1200 °C (Fig. 3c) shows poorest microstructure. Fig. 3b indicates SSC cathode sintered at 1100 °C results in a microstructure with both reasonable porosity and strong adhesion to the electrolyte. The optimum sintering condition is chosen to be 1100 °C for 5 h. As is evident in Fig. 3d, the addition of SNDC into SSC results in improvement of cathode microstructure, enhancement of interface adhesion to the electrolyte and particle connection.

3.2. Area specific resistances

Fig. 4 presents the impedance spectra of SSC–SNDC30 cathode recorded in atmospheric pressure ($P_{O_2} = 0.21$ atm) under open-circuit voltage (OCV) state. Area specific resistance (ASR) of the symmetrical cathode can be calculated as follows:

$$\text{ASR} \ (\Omega\,\text{cm}^2) = \frac{AR_i}{2} \qquad (2)$$

where A is the effective electrode area, R_i is the resistance originated from a.c. impedance spectrum, e.g. R_M represents the electrode resistance obtained from a.c. impedance spectrum in the medium-frequency range. As shown in Fig. 4, the ASR is as low as 0.34 Ω cm^2 at 700 °C. Impedance spectra take on depressed arcs, in which three different contributions can be clearly distinguished. The impedance spectra can be fitted using an equivalent circuit. However, the problem for equivalent circuit is raised from that one impedance spectrum can be fitted well by different equivalent circuits, giving different physical meanings [20,21]. In this work, the impedance spectra are fitted using an equivalent circuit with the configuration of $L_1 R_1 (C_1 (R_2 (\text{CPE}_1 R_3)))$ based on the previous research [13,15,20–22]. L_1 is the inductance; R_1 is the electrolyte ohmic resistance in high-frequency range; C_1 is the interfacial capacity; CPE$_1$ is the constant phase element; R_2 and R_3 are the electrode interfacial polarization resistances at medium-frequency and low-frequency range.

Fig. 5 shows the temperature dependence of ASR values for different cathodes. For SSC cathode, the lowest ASRs are yielded when it is sintered at 1100 °C for 5 h, which are in good agreement with the SEM reports. The ASRs for SSC–SNDC30 cathode are much lower than those of SSC. The activation energies for SSC and SSC–SNDC30 are 1.493 eV and 0.976 eV, respectively. The incorporation of SNDC greatly improves the performance of SSC cathode.

3.3. Possible oxygen reduction reaction (ORR) mechanism

The following processes involved in the ORR on mixed ionic and electronic conductors (MIECs) are widely accepted based on previous research [12,13,15,19,22–25]:
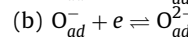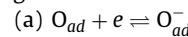
(i) Adsorption of O_2 onto the cathode surface:

$$O_{2,gasphase} \rightleftharpoons O_{2,ad}$$
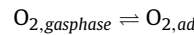
(ii) Dissociation of molecular adsorbed oxygen into atom adsorbed oxygen on cathode surface:

$$O_{2,ad} \rightleftharpoons 2O_{ad}$$
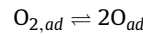
(iii) Reduction reaction of atom adsorbed oxygen into adsorbed oxygen ion on cathode surface:
(a) $O_{ad} + e \rightleftharpoons O_{ad}^-$
(b) $O_{ad}^- + e \rightleftharpoons O_{ad}^{2-}$

(iv) Transfer of surface adsorbed oxygen ion to three phase boundaries (TPBs):

$$O_{ad}^{2-} \rightleftharpoons O_{TPBs}^{2-}$$
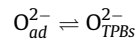
(v) Charge-transfer reaction at TPBs:

$$O_{TPBs}^{2-} + V_O^{\bullet\bullet} \rightleftharpoons O_O^X$$
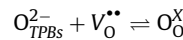
In parallel, steps (vi)–(viii) could also occur, competing with steps (iii)–(v):

(vi) Surface diffusion of atom adsorbed oxygen to the TPBs:

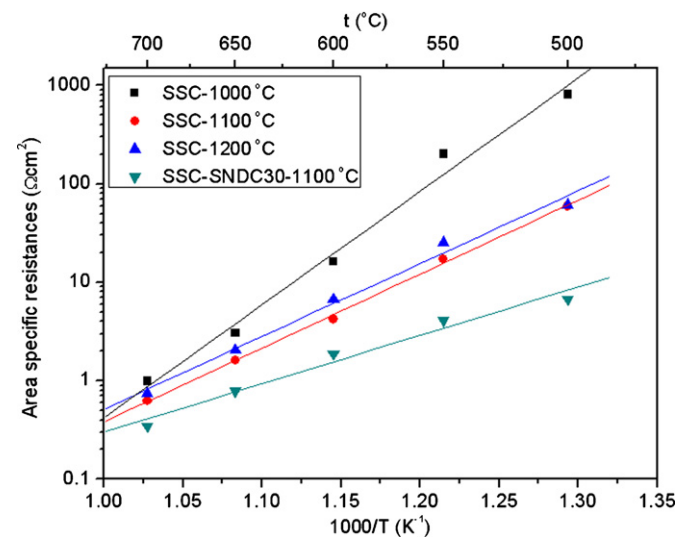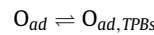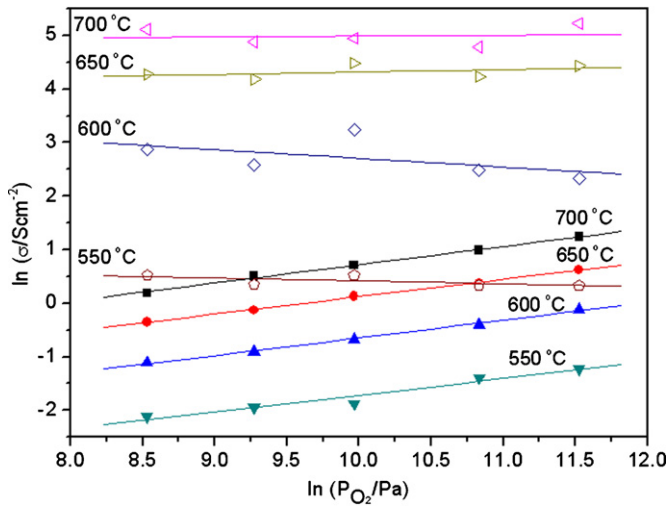$$O_{ad} \rightleftharpoons O_{ad,TPBs}$$

Fig. 5. Dependency of area specific resistances on temperatures for different cathodes.

Fig. 6. Dependency of specific electrode conductivities on oxygen partial pressures (P_{O_2}) for SSC–SNDC30 cathode at various temperatures.

(vii) Reduction reaction of atom adsorbed oxygen into adsorbed oxygen ion at TPBs:
  (a) $O_{ad,TPBs} + e \rightleftharpoons O^-_{ad,TPBs}$
  (b) $O^-_{TPBs} + e \rightleftharpoons O^{2-}_{TPBs}$
(viii) Charge-transfer reaction at TPBs:

$$O^{2-}_{TPBs} + V^{\bullet\bullet}_O \rightleftharpoons O^X_O$$

The reactions in steps (vii) and (viii) can also be combined into one total reaction shown in step (ix):

(ix) $O_{ad,TPBs} + 2e + V^{\bullet\bullet}_O \rightleftharpoons O^X_O$
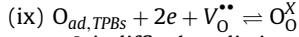
It is difficult to distinguish step (ix) and steps (vii)–(viii), since they exhibit the same characteristics.

(x) The total ORR can be written in step (x):

$$O_{2,gasphase} + 4e + 2V^{\bullet\bullet}_O \rightarrow 2O^X_O$$
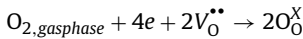
where $O_{2,gasphase}$, $O_{2,ad}$, O_{ad}, O^-_{ad}, $O_{ad,TPBs}$, $O^-_{ad,TPBs}$, O^{2-}_{TPBs}, $V^{\bullet\bullet}_O$ and O^X_O represents molecular oxygen in gas phase, molecular adsorbed oxygen, atom adsorbed oxygen on surface, surface adsorbed O^- ion, atom adsorbed oxygen at TPBs, adsorbed O^- ion at TPBs, O^{2-} ion at TPBs, oxygen vacancies and oxygen ions in electrolyte, respectively. Steps (iii), (iv), (vii), (ix) might be the rate determining steps (RDSs) in the overall ORR on cathode.

In our equivalent circuit in Fig. 4, medium-frequency resistance feature might be raised from reduction reaction of atom adsorbed oxygen into adsorbed oxygen ion (step (iii)), transfer of surface adsorbed oxygen ion to three phase boundaries (TPBs) (step (iv)), surface diffusion of atom adsorbed oxygen (step (vi)) and transport of oxygen ions across the cathode/electrolyte interface (step (v) or (viii)).

We define specific electrode conductivity for each electrode process:

$$\sigma_i = \frac{1}{AR_i} \tag{3}$$

where σ_i is the specific electrode conductivity, e.g. σ_M is the specific electrode conductivity originated from a.c. impedance spectrum in the medium-frequency range. The specific electrode conductivities varying with oxygen partial pressures at different temperatures are shown in Fig. 6, from which, dependencies of specific electrode conductivities on P_{O_2} are calculated and presented in Table 1.

Table 1
Dependencies of electrode conductivities on oxygen partial pressures at different temperatures.

t (°C)	σ_M	σ_L
700	0.0156	0.341
650	0.0450	0.325
600	−0.161	0.330
550	−0.0539	0.313

The relationship between the specific electrode conductivity (σ_i) and oxygen partial pressure (P_{O_2}) can be given by Eq. (4):
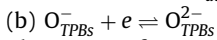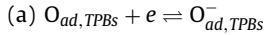
$$\sigma_i \propto P^n_{O_2} \tag{4}$$

Medium-frequency conductivities show no dependency on P_{O_2}. Table 2 summarizes the elementary reactions and the corresponding reaction orders. The adsorption/desorption process on the cathode surface and diffusion of adsorbed oxygen atoms has a dependency of 0.5 on P_{O_2} [14,16,21,26], the conduction of oxygen ions in the bulk cathode exhibits a dependency of 1/4 on P_{O_2}, since the ionic conductivity of the cathode is determined by the oxygen vacancy concentrations [7]. Consequently, the medium-frequency conductivities can only be attributed to the oxygen ions transfer across the electrode/electrolyte interface. $(La_{0.82}Sr_{0.18})_{0.82}MnO_3$ (LSM) cathode also exhibits similar phenomena in medium-frequency range using same nested RC equivalent circuit [20]. The dependencies of low-frequency conductivities on P_{O_2} vary in the range from *ca.* 0.31 to *ca.* 0.34 and increase with increasing temperatures. The nested RC equivalent circuit demonstrates two interrelated limiting electrode processes; however, it also has limitation due to its low distinguishability with respect to P_{O_2}. Therefore, we cannot simply and directly assign the single element of equivalent circuit to distinct physical process [21]. It is reasonable to extrapolate that the low-frequency electrode process is a mixing process involving oxygen reduction reaction related to atomic oxygen (step (iii-a) or step (vii-a)) with reaction order of 3/8 and oxygen ions conduction process (step (iv)) together with total charge-transfer process (step (ix)) with reaction order of 1/4 into RDSs. At 700 °C, the reaction order n equals to 0.341, approaching to 3/8. It indicates that the oxygen reduction reaction related to atomic oxygen (step (iii) or step (vii)) participates in the RDS and plays a predominant role, since the oxygen surface exchange kinetics, oxygen ion bulk conduction and total charge-transfer process have been enhanced at high temperatures. At 550 °C, the reaction order n equals to 0.313, approximately approaching to 1/4, which shows that oxygen ions conduction process (step (iv)) and total charge-transfer process (step (ix)) may involve in the RDSs and dominate. This is because the ohmic polarization increases with decreasing temperatures, which lowers the oxygen ion conductivity. The low-frequency capacitance can be calculated from Eq. (5),
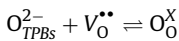
Table 2
Elementary reactions and corresponding reaction orders.

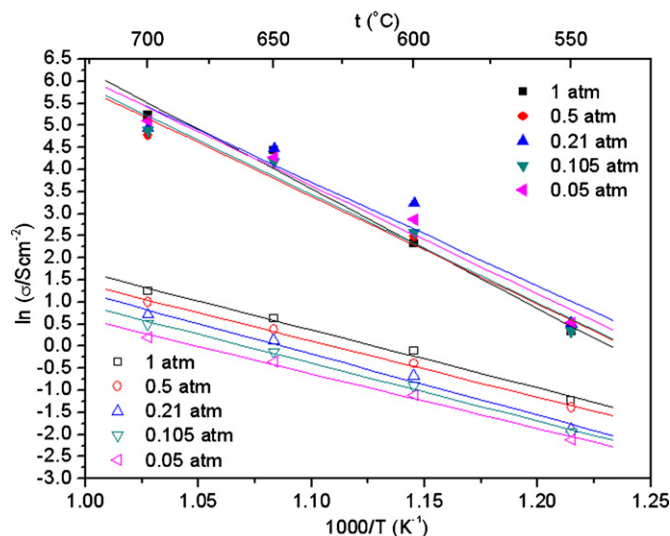| Elementary reactions	Reaction orders (n)
(i) $O_{2,gasphase} \rightleftharpoons O_{2,ad}$	1
(ii) $O_{2,ad} \rightleftharpoons 2O_{ad}$	1
(iii-a) $O_{ad} + e \rightleftharpoons O^-_{ad}$	3/8
(iii-b) $O^-_{ad} + e \rightleftharpoons O^{2-}_{ad}$	1/8
(iv) $O^{2-}_{ad} \rightleftharpoons O^{2-}_{TPBs}$	1/4
(v) $O^{2-}_{TPBs} + V^{\bullet\bullet}_O \rightleftharpoons O^X_O$	0
(vi) $O_{ad} \rightleftharpoons O_{ad,TPBs}$	1/2
(vii-a) $O_{ad,TPBs} + e \rightleftharpoons O^-_{ad,TPBs}$	3/8
(vii-b) $O^-_{TPBs} + e \rightleftharpoons O^{2-}_{TPBs}$	1/8
(ix) $O_{ad,TPBs} + 2e + V^{\bullet\bullet}_O \rightleftharpoons O^X_O$	1/4

Fig. 7. Dependency of specific electrode conductivities on temperatures for SSC–SNDC30 cathode under various oxygen partial pressures (P_{O_2}).

where C_L is the low-frequency capacitance, R_L is the low-frequency resistance, Q_L is the low-frequency pseudocapacitance [27].

$$C_L = \frac{(R_L Q_L)^{1/n}}{R_L} \qquad (5)$$

The low-frequency capacitances vary between 0.077 F cm^{-2} and 0.366 F cm^{-2}, which are reasonable for our ratiocination on the low-frequency electrode process. Based on the above analysis, we can make the conclusion that the RDSs occur two times in the whole ORR, since step (iii) and step (vii) have the same possibility to occur and it cannot be distinguished at this stage, so are step (iv) and step (ix).

Fig. 7 presents the temperature dependence of medium-frequency and low-frequency electrode conductivities under various oxygen partial pressures. The medium-frequency conductivities exhibit no dependency on the oxygen partial pressures. This indicates that the medium-frequency electrode process might be associated with the oxygen ions transfer across the electrode/electrolyte interface. On the contrary, the low-frequency conductivities increase with the increasing P_{O_2}. It indicates that low-frequency electrode process presumably originates from the oxygen exchange reaction at the gas/electrode interface [13,22,28–30]. The calculated activation energies are shown in Table 3. The activation energies of E_M and E_L are around 2.03–2.33 eV and 1.07–1.19 eV, respectively. Both the medium-frequency and low-frequency activation energies are independent of P_{O_2}.

3.4. Determination of oxygen reduction reaction (ORR) kinetics

IR-compensated current density (i)–overpotential (η) relationship is presented in Fig. 8. For a specific overpotential, the current density is observed to increase with the operating temperature, indicating the electrochemical activity of the SSC–SNDC30 cathode at high temperature is superior to that of low temperature. The cur-
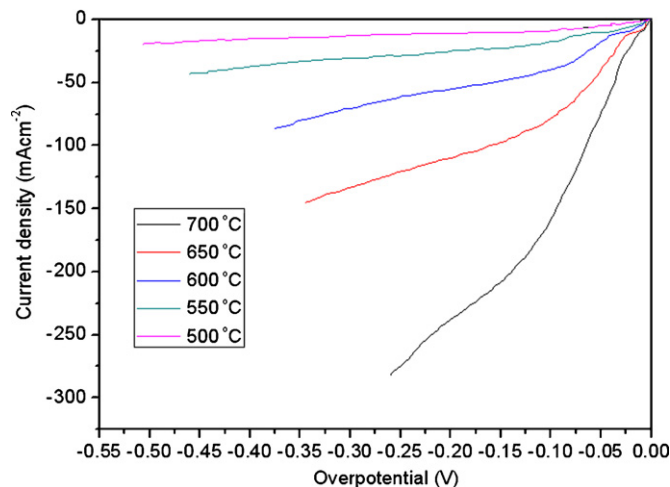

Fig. 8. IR-compensated current density (i)–overpotential (η) relationship (5 mV s^{-1}) of the ORR on SSC–SNDC30 cathode at various temperatures in air.

rent density can keep stable even the applied overpotential extends to relatively negative value of -500 mV. It verifies that the negative overpotential does not cause any deleterious effect on the electrochemical activity of the cathode. Fig. 9 presents the Tafel plots of the data originated from Fig. 8.

The well-known Butler–Volmer equation can be expressed as:

$$i = i_o \left[exp\left(\frac{\alpha_a F \eta}{RT}\right) - \exp\left(\frac{-\alpha_c F \eta}{RT}\right) \right] \qquad (6)$$

where

$$\alpha_a + \alpha_c = \frac{n}{\nu} \qquad (7)$$

for the ORR:

$$\alpha_c = \frac{\gamma}{\nu} + r\beta \qquad (8)$$

In the above equations, i is the measured current density for the ORR, α_a is the anodic transfer coefficient, α_c is the cathodic transfer coefficient, η is the overpotential, n is the total electron numbers transferred in the ORR, ν is the number of times that RDS occurs for one full ORR reaction, γ is the number of electrons transfers before the RDS, r is the number of electrons transfers in the RDS, β is the symmetry coefficient of the RDS, which is always assumed to be

Table 3
Activation energies of electrode conductivities of medium-frequency arcs (E_M) and low-frequency arcs (E_L) under different oxygen partial pressures.

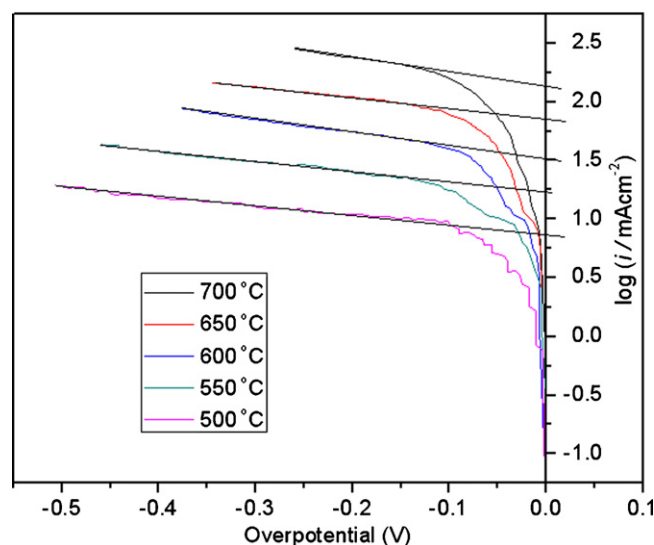|	1 atm	0.5 atm	0.21 atm	0.105 atm	0.05 atm
E_M (eV)	2.33	2.10	2.03	2.12	2.11
E_L (eV)	1.13	1.10	1.19	1.13	1.07

Fig. 9. Tafel plots of the ORR on SSC–SNDC30 cathode (data from Fig. 8).

Table 4
Comparison of i_o values of ORR on SSC–SNDC30 cathode and SG-LSCF cathode.

t (°C)	i_o (high-field) (mA cm^{-2})		i_o (low-field) (mA cm^{-2})		i_o (impedance spectra) (mA cm^{-2})	
	SSC–SNDC30	SG-LSCF	SSC–SNDC30	SG-LSCF	SSC–SNDC30	SG-LSCF
700	134.68	13	46.68	60	54.84	65
650	70.99	–	25	–	26.92	–
600	31.72	4	15.8	12.5	10.4	13
550	17.14	–	8.74	–	5.6	–

0.5, F, R and T are Faraday constant, ideal gas constant and absolute temperature, respectively [24].

The exchange current density, i_o, indicates the intrinsic electrochemical activity of cathode and ORR rate. It can be yielded by using the high-field and low-field approximations to the Butler–Volmer equation and charge-transfer resistance (R_{ct}) from a.c. impedance data.

For low-field approximations, i_o can be obtained from the slope of current density (i)–overpotential (η) relationship:

$$i_o = \frac{RT\nu}{nF}\text{slope} \tag{9}$$

Eq. (9) can be reasonable, provided that the linear low-field region is ± 27 mV at 500 °C, ± 28 mV at 550 °C, ± 30 mV at 600 °C, ± 32 mV at 650 °C and ± 34 mV at 700 °C, respectively, so that the relative error is less than 2% [24].

For high-field approximations, i_o can be readily calculated using Eq. (10):

$$\log\ i = \log i_o - \frac{\alpha_c F}{2.3RT}\eta \tag{10}$$

With the aim of minimizing the relative error to less than 1%, the minimum overpotential should exceed 153 mV at 500 °C, 163 mV at 550 °C, 173 mV at 600 °C, 183 mV at 650 °C and 193 mV at 700 °C, respectively, to reach the linear Tafel region, assuming reaction mechanism with $\nu = 2$, $n = 4$, according to our previous analysis in Section 3.3.

Eq. (11) can be approximately established in the low-field approximations:

$$\frac{i}{\eta} = \frac{1}{R_{ct}} \tag{11}$$

where R_{ct} represents the charge-transfer resistance obtained from impedance data under OCV state.

Consequently, Eq. (9) can be expressed as:

$$i_o = \frac{RT\nu}{nF}\frac{1}{R_{ct}} \tag{12}$$

Table 4 presents the i_o values from Eq. (9), (10) and (12). All the i_o values for ORR on SSC–SNDC30 cathode are observed to increase with the increasing temperature. Values of i_o for ORR originated from low-field approximation are quite similar to the values obtained from a.c. impedance data. The i_o values originated from high-field approximations are much higher than those of low-field approximations and a.c. impedance data under OCV state. It demonstrates the polarization overpotential has great effect on the kinetics of ORR. This phenomenon clearly indicates the charge-transfer reactions (step (v), step (viii) and step (ix)) is electrochemical in nature and plays a dominant role in the whole ORR, which could most likely be the RDSs under high cathodic overpotential. However, under low-field or near equilibrium condition, the disassociative adsorption of oxygen (step (ii)) and the diffusion of oxygen atoms (step (vi)) are presumably involved into the RDSs. The i_o values for ORR at single phase sol–gel derived

La$_{0.8}$Sr$_{0.2}$Co$_{0.8}$Fe$_{0.2}$O$_3$ (SG-LSCF) are also shown in Table 4 for comparison [31]. It is observed that the SSC–SNDC30 cathode possesses higher i_o values than that of SG-LSCF in the high-field approximations, indicating the electrochemical activity and ORR rate of SSC–SNDC30 cathode is superior to that of SG-LSCF cathode under high cathodic polarization. It again certifies that the charge-transfer reactions involve in the RDSs under high cathodic overpotential. The incorporation of SNDC into the SSC cathode greatly extends the active reaction zone of TPBs, where most charge-transfer reactions occur. However, SSC–SNDC30 cathode exhibits lower i_o values than that of SG-LSCF in the low-field approximations or in a.c. impedance spectra near equilibrium state. It agrees well with our conclusion that the disassociative adsorption of oxygen (step (ii)) and the diffusion of oxygen atoms (step (vi)) are the RDSs since the incorporation of SNDC reduces the active area of SSC for the disassociative adsorption and diffusion of oxygen atoms.

The dependency of equilibrium exchange current density on P_{O_2} can be expressed [32]:

$$i_o = (P_{O_2})^m \tag{13}$$

in which equilibrium exchange current density is obtained from Eq. (12) originated from a.c. impedance data under OCV state. m is closely related to electrons transferring in the RDSs. If the electrons transfer to atomic oxygen, m can be expressed:

$$m = \frac{\alpha_a}{2(\alpha_a + \alpha_c)} \tag{14}$$

in which α_a and α_c represent the anodic and cathodic charge transfer coefficient [33].

As shown in Fig. 10, the m value is observed to increase with the increasing temperature. m equals to 0.27 at 550 °C, which approximately approaches to 1/4, indicating the total charge-
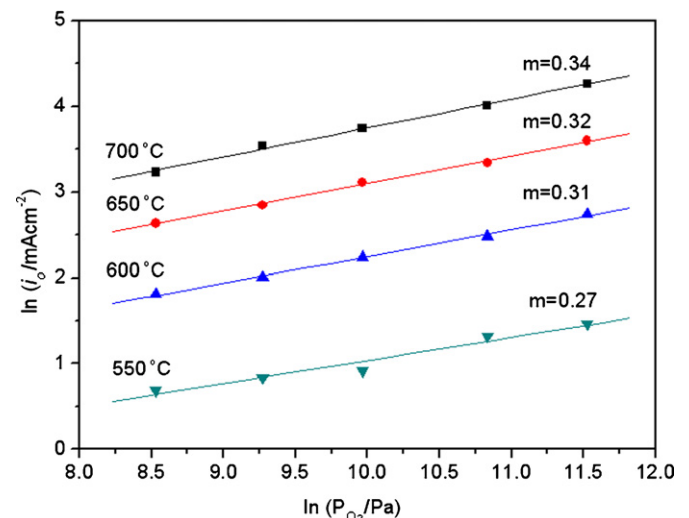
Fig. 10. Dependency of exchange current densities on oxygen partial pressures (P_{O_2}) for SSC–SNDC30 cathode at various temperatures.
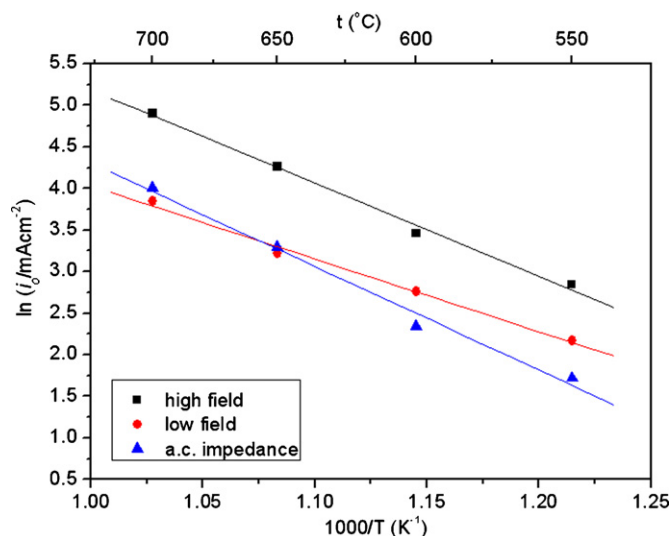
Fig. 11. Dependency of exchange current densities on temperatures for SSC–SNDC30 cathode obtained from different methods.

transfer process (step (ix)) involves in the RDSs since the α_a and α_c equals to unity. m increases to 0.34 at 700 °C, which approximately approaches to 3/8, illustrating the oxygen reduction reaction related to atomic oxygen (step (iii-a) or step (vii-a)) is the RDSs [32,34,35]. These results are in good accordance with the analysis of Fig. 6. It indicates that our proposed mechanism for the ORR on SSC–SNDC30 cathode is quite reasonable.

Fig. 11 illustrates the temperature dependence of i_o values for ORR on SSC–SNDC30 cathode using different techniques. The ORR activation energies obtained from Fig. 11 are summarized in Table 5, in which the ORR activation energies for SG-LSCF are also presented. The ORR activation energies of SSC–SNDC30 cathode are much lower than those of SG-LSCF cathode and composites of LSCF and GDC [36], indicating the SSC–SNDC30 cathode possesses much higher electrochemical activity.

3.5. Stability of the cathode

Fig. 12 presents the long-term stability of SSC–SNDC30 cathode under constant polarization voltage of −0.4 V vs. OCV, indicating the SSC–SNDC30 cathode can keep essentially stable over 52 h. There is a rather rapid activation process in the first 20 min with the application of cathodic polarization. Consistently, a dramatic decrease in the electrode polarization resistance is observed [37]. This behavior could be attributed to the elimination of passivated SrO on SSC surface [38]. The polarization current gradually increases with time, which can be ascribed to the activation process of interface between the cathode and electrolyte, corresponding to the minor decrease in electrode polarization resistance. The activation process is assumed to be closely related to the propagation process of oxygen vacancies from SSC/SNDC interface at the initial stage to the whole internal and external surface through grain boundary. Co ions are reduced under cathodic polarization, resulting in extraction of interstitial

Table 5
Comparison of activation energy of the ORR at different cathodes.

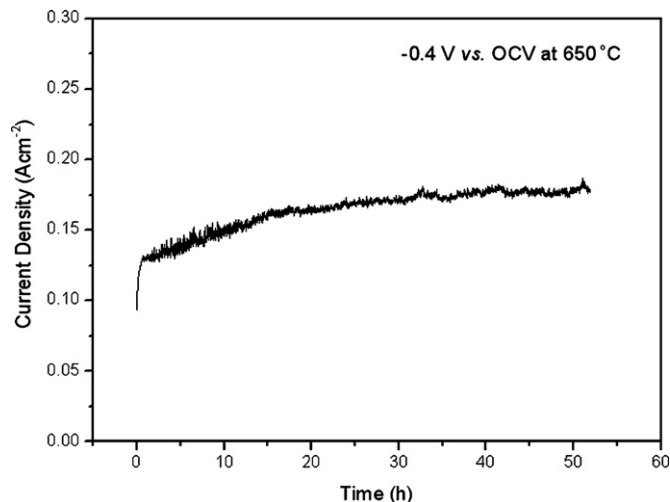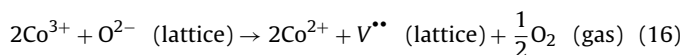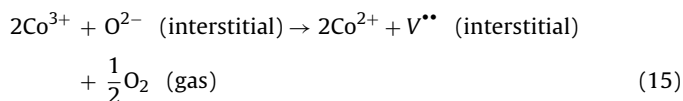|	E_a (eV) of SSC–SNDC30	E_a (eV) of SG-LSCF
High-frequency field	0.964	1.35
Low-frequency field	0.757	1.402
a.c. impedance	1.075	1.09

Fig. 12. Long-term stability measurement for SSC–SNDC30 cathode under constant polarization voltage of −0.4 V vs. OCV at 650 °C.

oxygen ions from SSC cathode for charge compensation [39]:

$$2Co^{3+} + O^{2-} \; (interstitial) \rightarrow 2Co^{2+} + V^{\bullet\bullet} \; (interstitial) + \frac{1}{2}O_2 \; (gas) \tag{15}$$

$$2Co^{3+} + O^{2-} \; (lattice) \rightarrow 2Co^{2+} + V^{\bullet\bullet} \; (lattice) + \frac{1}{2}O_2 \; (gas) \tag{16}$$

where $V^{\bullet\bullet}$ indicates oxygen vacancies in the interstitial or lattice sites. The formation of oxygen vacancies is responsible for electrochemical activity enhancement of SSC–SNDC30 cathode presumably resulting from extension the active reaction zone from TPBs to the cathode surface [39–42]. The exchange current densities obtained from high-field approximation are much higher than that originated from low-field approximation or a.c. impedance spectrum at OCV state according to our previous calculation in Section 3.4, which is in accordance with our results. Evidently, the high polarization voltage does not cause any degradation and deleterious effect to the morphology and adhesion of the interface. These results indicate that the SSC–SNDC30 cathode has excellent long-term stability and is suitable for application in SOFCs based on SNDC electrolyte.

4. Conclusions

SSC has been investigated as promising cathode material for SOFCs based on SNDC electrolyte. XRD and SEM techniques are employed to characterize the SSC cathode. Area specific resistances of SSC–SNDC30 cathode are much lower than those of SSC cathode after being sintered at 1100 °C for 5 h. Possible ORR mechanism has been proposed for the SSC–SNDC30 cathode. Medium-frequency conductivities have no dependency on P_{O_2}, which can be attributed to the oxygen ions transfer across the electrode/electrolyte interface. The low-frequency electrode process is a mixing process involving oxygen reduction reaction related to atomic oxygen and oxygen ions conduction process together with total charge-transfer process. The exchange current densities i_o from high-field approximations are much higher than those of low-field approximations and a.c. impedance data under OCV state, indicating the polarization overpotential has great effect on the kinetics of ORR. The SSC–SNDC30 cathode exhibits excellent long-term stability. The polarization current increases with time, which can be ascribed to the propagation process of oxygen vacancies. These results indicate

the SSC–SNDC30 cathode is highly promising for SOFCs with SNDC electrolyte.

Acknowledgements

References

[1] Z.P. Shao, S.M. Haile, Nature 431 (2004) 170–173.
[2] B.C.H. Steele, A. Heinzel, Nature 414 (2001) 345–352.
[3] J.S. Ahn, S. Omar, H. Yoon, J.C. Nino, E.D. Wachsman, J. Power Sources 195 (2010) 2131–2135.
[4] S. Omar, E.D. Wachsman, J.C. Nino, Solid State Ionics 177 (2006) 3199–3203.
[5] S. Omar, E.D. Wachsman, J.C. Nino, Solid State Ionics 178 (2008) 1890–1897.
[6] W. Zhou, Z.P. Shao, R. Ran, W.Q. Jin, N.P. Xu, Chem. Commun. 44 (2008) 5791–5793.
[7] C.R. Xia, W. Rauch, F.L. Chen, M.L. Liu, Solid State Ionics 149 (2002) 11–19.
[8] J. Chen, F.L. Liang, B. Chi, J. Pu, S.P. Jiang, L. Jian, J. Power Sources 194 (2009) 275–280.
[9] J. Chen, F.L. Liang, L.N. Liu, S.P. Jiang, B. Chi, J. Pu, J. Li, J. Power Sources 183 (2008) 586–589.
[10] F.L. Liang, J. Chen, S.P. Jiang, B. Chi, J. Pu, L. Jian, Electrochem. Solid State Lett. 11 (2008) B213–B216.
[11] F.L. Liang, J. Chen, S.P. Jiang, B. Chi, J. Pu, L. Jian, Electrochem. Commun. 11 (2009) 1048–1051.
[12] S.W. Baek, J. Bae, Y.S. Yoo, J. Power Sources 193 (2009) 431–440.
[13] F.S. Baumann, J. Maier, J. Fleig, Solid State Ionics 179 (2008) 1198–1204.
[14] S.B. Adler, J.A. Lane, B.C.H. Steele, J. Electrochem. Soc. 143 (1996) 3554–3564.
[15] S.Z. Wang, T. Chen, S.P. Chen, J. Electrochem. Soc. 151 (2004) A1461–A1467.
[16] M. Koyama, C.J. Wen, T. Masuyama, J. Otomo, H. Fukunaga, K. Yamada, K. Eguchi, H. Takahashi, J. Electrochem. Soc. 148 (2001) A795–A801.
[17] D. Beckel, U.P. Muecke, T. Gyger, G. Florey, A. Infortuna, L.J. Gauckler, Solid State Ionics 178 (2007) 407–415.
[18] J. Winkler, P.V. Hendriksen, N. Bonanos, M. Mogensen, J. Electrochem. Soc. 145 (1998) 1184–1192.
[19] T. Horita, K. Yamaji, N. Sakai, H. Yokokawa, A. Weber, E. Ivers-Tiffee, Electrochim. Acta 46 (2001) 1837–1845.
[20] S.P. Jiang, J.G. Love, Y. Ramprakash, J. Power Sources 110 (2002) 201–208.
[21] C. Schwandt, W. Weppner, J. Electrochem. Soc. 144 (1997) 3728–3738.
[22] F.S. Baumann, J. Fleig, H.U. Habermeier, J. Maier, Solid State Ionics 177 (2006) 1071–1081.
[23] Y.H. Li, R. Gemmen, X.B. Liu, J. Power Sources 195 (2010) 3345–3358.
[24] A.C. Co, S.J. Xia, V.I. Birss, J. Electrochem. Soc. 152 (2005) A570–A576.
[25] W. Zhou, R. Ran, Z.P. Shao, R. Cai, W.Q. Jin, N.P. Xu, J. Ahn, Electrochim. Acta 53 (2008) 4370–4380.
[26] Y. Takeda, R. Kanno, M. Noda, Y. Tomida, O. Yamamoto, J. Electrochem. Soc. 134 (1987) 2656–2661.
[27] D.J. Chen, R. Ran, K. Zhang, J. Wang, Z.P. Shao, J. Power Sources 188 (2009) 96–105.
[28] F.S. Baumann, J. Fleig, G. Cristiani, B. Stuhlhofer, H.U. Habermeier, J. Maier, J. Electrochem. Soc. 154 (2007) B931–B941.
[29] F.S. Baumann, J. Fleig, H.U. Habermeier, J. Maier, Solid State Ionics 177 (2006) 3187–3191.
[30] F.S. Baumann, J. Fleig, M. Konuma, U. Starke, H.U. Habermeier, J. Maier, J. Electrochem. Soc. 152 (2005) A2074–A2079.
[31] J.B. Liu, A.C. Co, S. Paulson, V.I. Birss, Solid State Ionics 177 (2006) 377–387.
[32] B.A. Vanhassel, B.A. Boukamp, A.J. Burggraaf, Solid State Ionics 48 (1991) 139–154.
[33] A.J.A. Winnubst, A.H.A. Scharenborg, A.J. Burggraaf, Solid State Ionics 14 (1984) 319–327.
[34] B.A. Vanhassel, B.A. Boukamp, A.J. Burggraaf, Solid State Ionics 48 (1991) 155–171.
[35] K. Kalimeri, G. Pekridis, S. Vartzoka, C. Athanassiou, G. Marnellos, Solid State Ionics 177 (2006) 979–988.
[36] E.P. Murray, M.J. Sever, S.A. Barnett, Solid State Ionics 148 (2002) 27–34.
[37] W. Wang, S.P. Jiang, J. Solid State Electrochem. 8 (2004) 914–922.
[38] S.P. Jiang, J.G. Love, Solid State Ionics 138 (2001) 183–190.
[39] H.Y. Lee, W.S. Cho, S.M. Oh, H.D. Wiemhofer, W. Gopel, J. Electrochem. Soc. 142 (1995) 2659–2664.
[40] T. Horita, K. Yamaji, N. Sakai, H. Yokokawa, T. Kawada, T. Kato, Solid State Ionics 127 (2000) 55–65.
[41] S.Z. Wang, Y. Jiang, Y.H. Zhang, J.W. Yan, W.Z. Li, J. Electrochem. Soc. 145 (1998) 1932–1939.
[42] Y. Jiang, S.Z. Wang, Y.H. Zhang, J.W. Yan, W.Z. Li, J. Electrochem. Soc. 145 (1998) 373–378.